





Article

Long-Term Water Quality Monitoring: Using Satellite Images for Temporal and Spatial Monitoring of Thermal Pollution in Water Resources

Reza Naimae^{1,*}, Abbas Kiani², Sina Jarahizadeh³, Seyed Babak Haji Seyed Asadollah^{3,4}, Pablo Melgarejo⁵ and Antonio Jodar-Abellan^{4,5}

¹ School of Surveying and Geospatial Engineering, College of Engineering, University of Tehran, Tehran 1439957131, Iran

² Department of Geomatics, Faculty of Civil Engineering, Babol Noshirvani University of Technology, Babol 4714871167, Iran

³ Department of Environmental Resources Engineering, State University of New York College of Environmental Science and Forestry (SUNY ESF), 1 Forestry Dr., Syracuse, NY 13210, USA; sjarahizadeh@esf.edu (S.J.); shajiseyedasadollah@esf.edu (S.B.H.S.A.)

⁴ Department of Civil Engineering, University of Alicante, 03690 Alicante, Spain; antonio.jodar@ua.es

⁵ Centro de Investigación e Innovación Agroalimentaria y Agroambiental (CIAGRO-UMH), Miguel Hernandez University, 03312 Orihuela, Spain; pablo.melgarejo@umh.es

* Correspondence: r.naimae@ut.ac.ir

Abstract: Thermal pollution reduces water quality through any process that leads to a change in the water's ambient temperature. Karun is one of the most relevant sources of water supply in Iran, and its pollution, created by industrial, urban, and agricultural issues, has been one of the most critical challenges throughout the last few years. As the water temperature rises, the amount of dissolved oxygen in it decreases, thereby affecting the entire ecosystem associated with it. Drainage of urban and industrial runoff into surface water sources can increase the water temperature. Dams also constitute a significant part, modifying spatial patterns of temperature along river routes and causing thermal contamination. In this paper, the thermal pollution of the Karun River was assessed, and regions along this river with unusually raised water temperatures were identified and compared over 20 years. By analyzing the results, it can be found that the thermal pollution from dams has a significant impact on the downstream river environment and ecology that is considerably relevant during summer periods, showing average decreases of 3 degrees Celsius immediately beyond the dams' locations (from 41 degrees Celsius upstream dams to 38 degrees Celsius beyond them) or even bigger (reductions of 13 degrees Celsius in one of the studied dams). Hence, our results showed that water temperature is colder downstream in the hot seasons of the year than upstream of the dams. The results suggest that the usage of remote sensing data effectively could complement collected data from ground-based sensors to estimate water temperature and to identify pollution areas. It provides experts with spatially extensive and highly synchronized data.

Keywords: water pollution; thermal imaging; dam; Landsat satellite; Karun River



Citation: Naimae, R.; Kiani, A.; Jarahizadeh, S.; Haji Seyed Asadollah, S.B.; Melgarejo, P.; Jodar-Abellan, A. Long-Term Water Quality Monitoring: Using Satellite Images for Temporal and Spatial Monitoring of Thermal Pollution in Water Resources. *Sustainability* **2024**, *16*, 646. <https://doi.org/10.3390/su16020646>

Academic Editor: Matteo Gentilucci

Received: 29 November 2023

Revised: 29 December 2023

Accepted: 5 January 2024

Published: 11 January 2024



Copyright: © 2024 by the authors. Licensee MDPI, Basel, Switzerland. This article is an open access article distributed under the terms and conditions of the Creative Commons Attribution (CC BY) license (<https://creativecommons.org/licenses/by/4.0/>).

1. Introduction

Over the past few decades, a significant portion of water resources, particularly those situated in close proximity to urban and industrial areas, has become polluted or is at a high risk of contamination [1]. As a consequence, the continuous and extensive monitoring of river water through both direct and indirect sampling approaches has become a vital criterion for planners and decision-makers in related disciplines [1,2]. One of the objectives in monitoring water systems is to initially manage and subsequently mitigate the current sources of pollution [3]. Extensive research has been undertaken to simulate water quality parameters, aiming to assess the extent of water pollution, including thermal pollution [4,5].

The thermal aspect is a crucial determinant of water quality due to its profound influence on various physical, chemical, and biological processes within aquatic ecosystems [6]. Temperature impacts the solubility of gases, affecting the availability of the dissolved oxygen that is critical for aquatic life. It also governs chemical reactions, bacterial activity, and the density of water, influencing nutrient cycling, organic matter decomposition, and water circulation [7]. Additionally, human-induced factors like thermal pollution can further exacerbate these effects, posing threats to water quality [7]. So, monitoring and managing water temperature are essential components of maintaining a sustainable and healthy aquatic environment.

Numerical models are one of the approaches used to solve this problem. Reference [8] investigated thermal contamination from a power plant utilizing the Irtysh River for cooling. A 2D numerical model was employed to simulate heated water discharge characteristics, demonstrating good alignment with the measured results. The research explored various scenarios of discharge, determining thermal pollution areas for different speeds. Ref. [9] introduced the mechanistic i-Tree Cool River Method, designed to identify causes and mitigation strategies for thermal pollution. The model estimates riparian shading effects based on vegetation characteristics and solar geometry. Along the New York Mountain River was demonstrated the sensitivity of this model to storm sewer and subsurface inflows, riparian shading, and upstream boundary temperatures, highlighting the model's effectiveness in assessing thermal pollution dynamics [9].

In water resources management, the quality assessment is considered a crucial factor, as it gives useful chemical information that could be used to solve possible problems and planning the management of reservoirs and rivers [2]. Nevertheless, achieving precise simulations necessitates the use of appropriate input data. Using in situ data sampling is both the common approach and a high-quality approach; however, based on numerous works from the literature, it is neither cost- nor time-efficient. With huge advancements in technology, remote sensing approaches are replacing the old methods, as they are more comprehensive, more accessible, and cheaper [10,11].

Landsat is a series of Earth-observing satellites that provide multispectral imagery for various applications, including environmental monitoring and resource management [12]. Its advantages include consistent global coverage, long-term data continuity, and the ability to capture images across different wavelengths. Landsat satellites are equipped with thermal and infrared sensors, extending their capabilities beyond visible-light imagery [12]. These sensors enable the detection of temperature variations and surface features not visible to the naked eye, allowing for an enhanced analysis of environmental conditions, such as identifying heat patterns, monitoring changes in land surface temperatures, and assessing vegetation health.

Landsat data were extensively utilized for thermal pollution, especially for areas near power plants, which are the most prone regions [13]. For example, Ref. [14] used Landsat data to analyze thermal anomalies subsequent to the Tianwan Nuclear Power Plant operation. The findings reveal a notable expansion of thermally polluted areas from 2001 to 2020 post-operation. The largest thermal pollution occurs in spring, followed by summer, winter, and autumn. Furthermore, Landsat observations were also used for river and reservoir pollutant monitoring. Ref. [15] proposed a remote sensing method using Landsat 8 imagery to detect thermal pollution around the Neka power plant, situated by the Caspian Sea. Utilizing Landsat 8's Operational Land Imager (OLI), along with thermal infrared remote (TIR) sensors, the research revealed a temperature rise in the power plant's water outlet channel, indicating potential environmental consequences from water thermal pollution. Reference [16] utilized the Landsat Enhanced Thematic Mapper Plus (ETM+) thermal infrared imagery to evaluate thermal waste induced by the Geheyan and Gaobazhou Dams on the Qingjiang River, a Yangtze River tributary. An analysis of 54 cloud-free Landsat ETM+ scenes from 2000 to 2014 revealed cooler water temperatures downstream of both dams during summer, with stable temperatures along the river in winter, indicating clear signs of dam-induced thermal pollution, affecting areas extending

over 20 km downstream of the Geheyan Dam and beyond the confluence of the Qingjiang and Yangtze Rivers for the Gaobazhou Dam [16].

Fazelpoor et al. [17] utilized MODIS satellite images to evaluate the water surface temperature and correlation with water depth in the Persian Gulf. The evaluation was performed at 250, 500, and 1000 m spatial resolutions. The results indicated that temperature variations, especially in the northern and central latitudes, have an inverse relationship with water depth. In other words, as the water depth increases, the temperature decreases, and vice versa [17]. Lopez and colleagues evaluated the sea surface temperature and salinity in coastal areas by utilizing Sentinel-2 data. They demonstrated that this method can be applied effectively in precise coastal and oceanographic applications [18]. Park and Jang retrieved the sea surface temperature by using 257 OLI image frames captured by a Landsat-8 satellite from 2013 to 2017. According to their research methodology, the root mean square error (RMSE) was approximately 0.59 centigrade and 0.72 centigrade. The results demonstrated the need for coastal areas to have high spatial-resolution satellite data [19].

The Karun River is one of the most significant surface water sources for Khuzestan State in Iran and, simultaneously, for the entire country. The watershed of this river encompasses at least five provinces in the country. Moreover, 90% of the water for industries, 70% of the population, and 60% of the agricultural lands in Khuzestan Province are supplied through this river [20]. Urban, industrial, and agricultural are the main Karun River thermal pollution sources [21]. The Karun River is severely contaminated by wastewater from industrial and agricultural facilities [22]. The industrial part of Karun River's thermal pollution is primarily associated with power stations and factories. They use Karun's water to reduce the temperature of cooling equipment and machinery [23]. Moreover, agricultural regions play a significant role in the thermal pollution of the Karun River. Considering the extensive agricultural activities, the pollution load of these activities is increasing. Returned water from agriculture, drinking, and aquaculture are the main pollution causes [19].

Another human activity that changes the hydrological processes in rivers is the construction of dams along rivers [16,24–26]. They play a crucial role in changing the spatial pattern of the temperature along the course of rivers, contribute significantly to thermal pollution, and exert a considerable impact on riverine aquatic ecosystems [24]. Specifically, the river water temperature often changes by dams [27,28]. A lot of studies have been conducted under various regions and weather conditions to understand the thermal effects of dams on downstream rivers. Among them, a study integrated remote sensing data and geographic information systems (GIS) to model the water-resource pollution of the Dez Dam [21]. For this purpose, they utilized ASTER sensor imagery, ground station information, electrical conductivity, and the temperature of the dam. Similarly, certain scientific studies assessed thermal changes in the water temperature after the Keepit Dam on the downstream river in Australia [29], the multipurpose dams of the Willamette River, and the Glen Canyon Dam in the Western United States [30,31]. Likewise, Paso de las Piedras Dam in Argentina [32] and the Geheyan, Gaobazhou, Three Gorges, and Danjiangkou Dams in China [16,33,34] were examples of activities that have evaluated the water temperature changes by dams.

Although some studies have measured thermal changes in dams downstream the rivers, these studies were conducted periodically rather than continuously. In addition, field measurements have certain limitations, including low spatial and temporal resolution, high cost, time-consuming procedures, and a lack of statistical distribution maps due to the limited number of observations. To overcome these limitations, we used satellite data to measure and analyze the changes in water temperature over consecutive years along the Karun River. More specifically, we assessed the impact of urban areas, industrial plants, agricultural fields, and dams on the thermal pollution of the Karun River over a period of 20 consecutive years (from 1999 to 2019).

2. Materials and Methods

2.1. Study Area

The Karun River, as depicted in Figures 1 and 2, holds a prominent status among the rivers in Khuzestan Province and stands as the largest and most abundant river in Iran, showing a total length of 950 km. Notably, it distinguishes itself as the sole river in the country, with a connection to international waters and oceans. Beyond its geographical significance (its basin encompasses a total area of 65,230 km²), the Karun River plays a vital role in providing essential resources to the region [21].

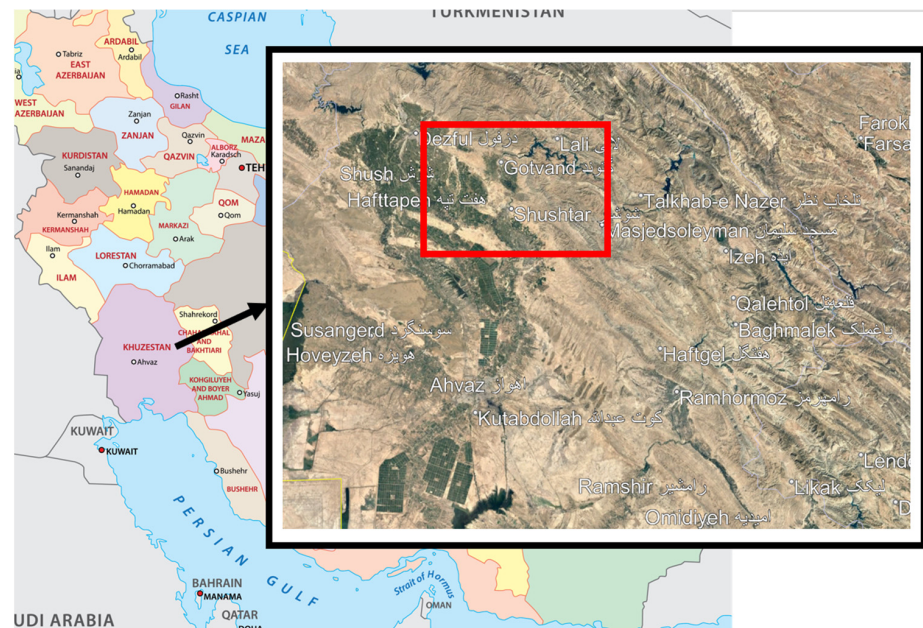


Figure 1. Location of Khuzestan Province on the map of Iran (red box represents the study area).

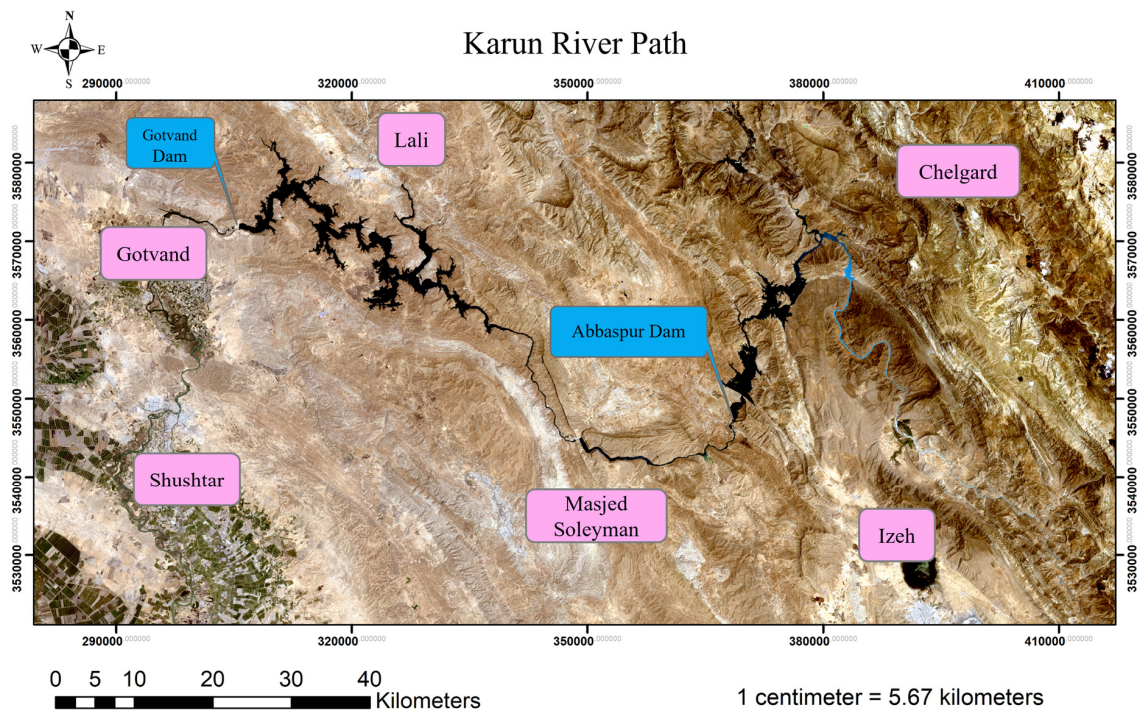


Figure 2. Dams in the northeastern province of Khuzestan and main cities (in pink boxes).

Functioning as a primary source of drinking water for Khuzestan Province, the majestic Karun River fulfills the water requirements of 16 cities, numerous villages, 65,000 hectares of agricultural land, and various industrial facilities [20]. Situated in the southwestern part of Iran, the Karun River spans approximately $48^{\circ}15'$ to $52^{\circ}15'$ latitude and $30^{\circ}17'$ to $33^{\circ}49'$ longitude. Its expansive reach and crucial contributions underscore its importance as a lifeline for the communities and industries it sustains [22].

Figure 2 shows a comprehensive view of the neighboring cities. The northeastern dams of Khuzestan Province are also shown in Figure 2. The Abbaspour Dam, also known as the Karun 1 Dam, is one of the largest dams in Iran, showing a total stored volume of 3140 km^3 . Located approximately 50 km northeast of Masjed Soleyman in Northern Khuzestan, it is a double-curve concrete dam. The construction of this dam, one of the earliest dams in Iran and the Middle East, began in 1965 and continued until 1975 [20,22].

The Masjed Soleyman Dam, or Karun 2 Dam, located in Khuzestan Province, is 25.5 km northeast of the city of Masjed Soleyman and 160 km northeast of Ahvaz, and is built on the Karun River. This dam belongs to the category of earth dams and has a current water volume of 0.261 km^3 . The Gotvand Dam is one of the largest dams in Iran, located on the Karun River in Northern Khuzestan. Located 380 km from the river's source, 25 km north of Shushtar and 10 km northeast of the city of Gotvand, it plays an important role in the region's water management thanks to its great capacity (4.5 km^3 according to [20,21]).

2.2. Landsat Imagery

In this study, Landsat-8 satellite images (from 2013 to present) were used to estimate the water temperature of the Karun River (Table 1). Thermal images were obtained from thermal bands within the wavelength ranges of (10.5–11.5 μm) and (11.5–12 μm), with a spatial resolution of 100 m. Although Landsat 7 has thermal bands with a spatial resolution of 60 m, Landsat-8 imagery was preferred. This choice was made because Landsat-7 has been subject to striping errors since 2003, and the use of neighboring pixels is recommended to address this issue. As the focus of this study is the Karun River, and the width of the river covers only a few pixels in the image, Landsat-7 images were not used. In addition, Landsat-5 imagery was used to compare temperature changes in the region over the past 20 years. Landsat-5 thermal imagery (1984–2012) covers the wavelength range of (10.4–12.5 μm), with a spatial resolution of 120 m (Table 1).

Table 1. Specifications of satellite images used in the present study.

Satellite	Sensors	Date	Time	Row	Column
Landsat 8	OLI/TIRS	2019/03/13	07:15:03	38	165
Landsat 8	OLI/TIRS	2019/07/22	07:15:27	38	165
Landsat 5	TM	1999/03/11	06:49:00	38	165
Landsat 5	TM	1999/07/17	06:52:12	38	165

2.3. Normalized Difference Water Index (NDWI)

The water threshold considered in remote sensing is based on the usage of pixel data, and by testing these data with each other, water particles are recognized. The use of automated methods to detect water in the study area is often limited to studies of groundwater or flowing water [2,3,5]. One of the reasons for choosing this method in reference studies is the lack of sufficient information on the spatial location of the water phenomenon under investigation.

Extracting water areas from satellite images is essential for various applications. Therefore, different techniques were used to achieve this goal in [35]. One of the most effective tested indices is the NDWI. This index is perhaps one of the most popular indices in remote sensing for identifying the spatial location of liquid water, and it is presented in one of the two methods below [36]. In this study, the NDWI was calculated within the most common method (Equation (1)), and this numerical expression resulted in being more

suitable to estimate the water mask of this place rather than the alternative method of NDWI estimation, as shown in Equation (2) [26,35,36].

$$\text{NDWI} = \frac{G - \text{NIR}}{G + \text{NIR}} \quad (1)$$

$$\text{NDWI} = \frac{\text{NIR} - \text{SWIR}}{\text{NIR} + \text{SWIR}} \quad (2)$$

where NDWI is the Normalized Difference Water Index, G depicts the reflectance in the green band, NIR represents the reflectance in the near-infrared band, and SWIR depicts the short-wave infrared channels or bands.

2.4. Brightness Temperature

The Earth's surface releases the maximum amount of energy at a wavelength of approximately 7.9 μm , constituting thermal infrared energy as a by-product of the Earth's heat [9–11]. Although this thermal radiation is invisible to the naked eye, it can be detected by thermal sensors like radiometers and scanners. The study of this thermal infrared region falls under the domain of thermal remote sensing, a specialized field in remote sensing that is dedicated to processing and interpreting data derived from this spectral range.

In essence, all materials emit electromagnetic waves when their surface temperature exceeds absolute zero. The quantity of energy emitted by each material correlates directly with its surface temperature. This fundamental relationship is encapsulated by the Stefan–Boltzmann law (Equation (3)) [37], providing a critical foundation for understanding the thermal behavior of materials and contributing to the principles governing thermal remote sensing.

$$E = \sigma \cdot T^4 \quad (3)$$

This equation states that the total energy emitted per unit area, E , is equal to the Stefan–Boltzmann constant, σ , multiplied by the fourth power of the absolute temperature, T , of the material in Kelvin [37].

Equation (3), known as the Stefan–Boltzmann law, is applicable when the material exhibits characteristics of a black body—a theoretical construct that absorbs all incident energy and re-emits it entirely. The wavelength at which a black body's radiation reaches its maximum intensity is intricately tied to the body's temperature, an association governed by Wien's displacement law (Equation (4)).

$$\lambda_{max} \cdot T = b \quad (4)$$

In Equation (4), λ_{max} is the wavelength at which the radiation is at its maximum; b is Wien's displacement constant, equal to 2898 μmK ; and T is the absolute temperature of the radiating material in Kelvin (K).

2.5. Radiometric Correction

Due to noise, shadows, and unwanted information in Landsat imagery, reflections of recorded phenomena are not true. In the direct registration of sensor reflections on Landsat series satellites, no effective measures were taken to reduce this unwanted information [38]. Under such conditions, the recorded digital numbers (DNs) do not accurately represent the true reflections of different land surface phenomena. By applying precise calibration coefficients to the images, it is possible to convert DN into Top of Atmosphere (TOA) reflectance values.

This information is used to calculate the brightness temperature from the TIRS thermal band sensor. To obtain the brightness temperature, the DN of each pixel is first converted to spectral radiance, using the calibration values provided. To convert the values of each pixel

in the images to the corresponding spectral radiance, Equation (5) is used for Landsat-8 images, and Equation (6) is used for Landsat-5 images [39].

$$L_{\lambda} = \text{gain} \times \text{DN} + \text{bias} \quad (5)$$

In Equation (5), L_{λ} represents the spectral radiance recorded by the TOA sensor corresponding to the wavelength, λ , measured in $[\text{W} \cdot \text{m}^2 \cdot \text{sr} \cdot \text{mm}]$. DN stands for the pixel values of the thermal image, and the parameters gain and bias are specific calibration factors for the Landsat-8 image band in consideration.

$$L_{\lambda} = \left(\frac{L_{\text{Max}} - L_{\text{Min}}}{Q_{\text{CalMax}} - Q_{\text{CalMin}}} \right) * \text{DN} + L_{\text{Min}} \quad (6)$$

Equation (6) features L_{λ} , denoting the spectral radiance recorded by the TOA sensor at the wavelength, λ , measured in $[\text{W} \cdot \text{m}^2 \cdot \text{sr} \cdot \text{mm}]$. DN signifies the pixel values of the thermal image. Additionally, Q_{CalMax} represents the maximum pixel value (255); Q_{CalMin} is the minimum pixel value (1); and L_{Max} and L_{Min} are, respectively, the minimum and maximum recorded spectral radiance values by the sensor in $[\text{W} \cdot \text{m}^2 \cdot \text{sr} \cdot \text{mm}]$.

2.6. Atmospheric Correction

Due to the effects of atmospheric scattering and absorption on the recorded energy, the TOA values differ from the actual reflections of ground surface phenomena [40]. Applying atmospheric corrections to surface reflections is essential in most cases, especially in multitemporal studies and extensive areas [41]. The impact of atmospheric absorption and scattering on the recorded DN of dark phenomena, including dense vegetation cover and water areas, is more pronounced [42]. In fact, the radiance in the atmosphere has atmospheric errors and requires correction, making it one of the crucial topics in satellite image processing. To estimate the surface water temperature, the atmospheric radiance is converted to the corrected surface radiance, using the following equation [42,43]:

$$L_{\lambda(T_s)} = \frac{L_{\lambda} - L_{\lambda}^{\text{up}}}{t \times \varepsilon_{\lambda}} - \frac{1 - \varepsilon_{\lambda}}{\varepsilon_{\lambda}} \times L_{\lambda}^{\text{down}} \quad (7)$$

In Equation (7), $L_{\lambda(T_s)}$ represents the corrected surface radiance, and L_{λ} represents the uncorrected surface radiance, calculated using Equations (5) and (6). L_{λ}^{up} and $L_{\lambda}^{\text{down}}$ denote the upward radiance or atmospheric path radiance and the downward radiance or sky radiance, respectively. Additionally, t and ε_{λ} represent atmospheric transmittance and surface emissivity, respectively [43,44].

3. Implementation and Results

The investigation utilized four satellite images, namely Landsat 8 and Landsat 5, corresponding to the summer and winter seasons of 20 years (from 1999 to 2019). The overall research trend is illustrated in Figure 3.

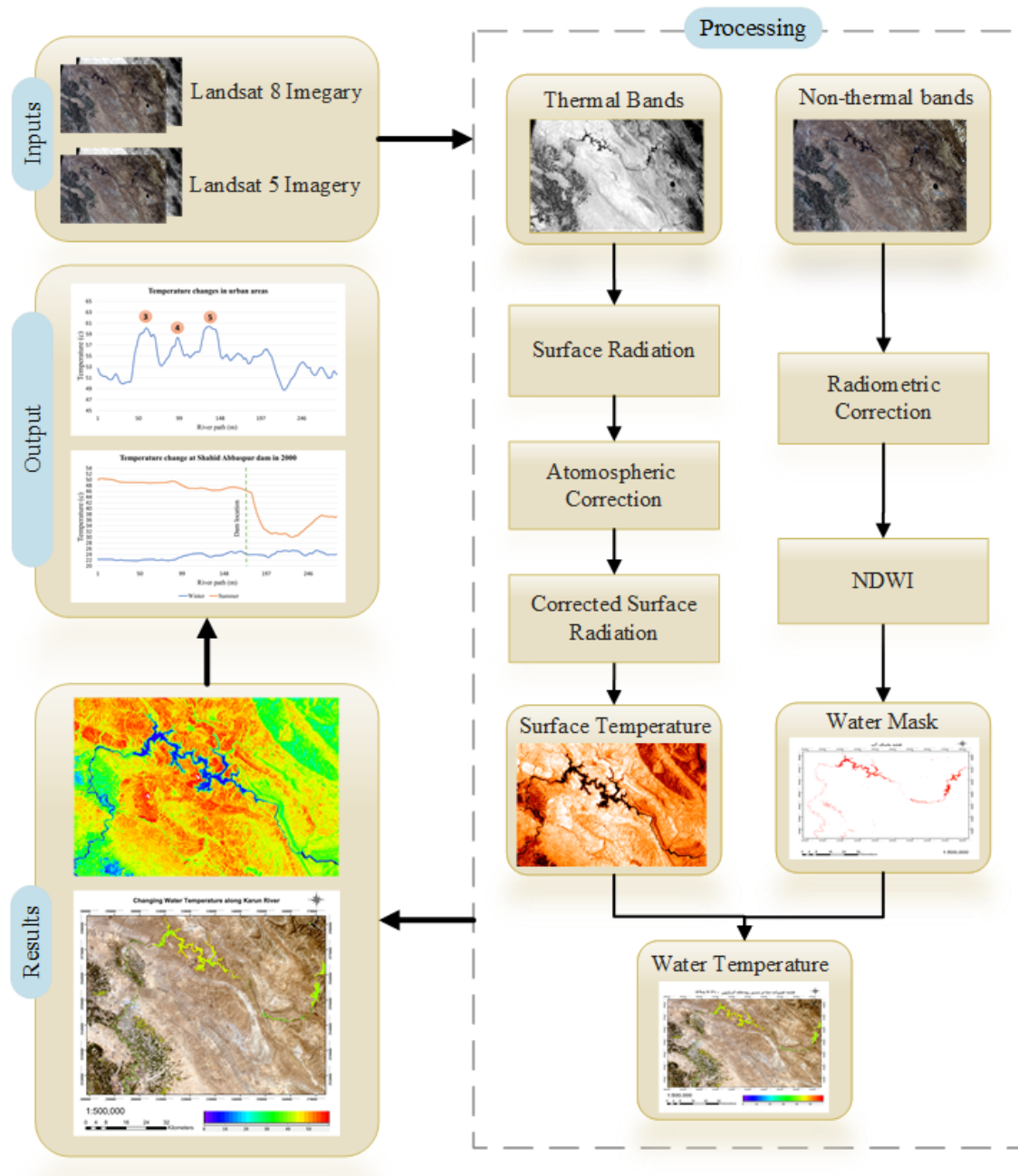


Figure 3. Proposed method output: Map showing regional temperature changes and identification of polluted areas. Evaluation includes a 20-year water temperature comparison and profiling temperature differences pre- and post-dam construction.

3.1. Implementation

In the initial step of estimating river water temperature, the generation of a water mask is essential. This task is performed using two methods: unsupervised classification and the NDWI technique [34–36].

- Unsupervised classification: Satellite data, specifically ISODATA (Iterative Self-Organizing Data Analysis Method (ISODATA)), were analyzed using the unsupervised classification technique. This method was applied to nonthermal bands with a cluster range of (2–5). The results are shown in Figure 4.

- Water index: Before calculating the water mask using the NDWI (Figure 5), radiometric corrections were applied to the visible bands, using calibration parameters. The implementation details are explained in Section 3.2.

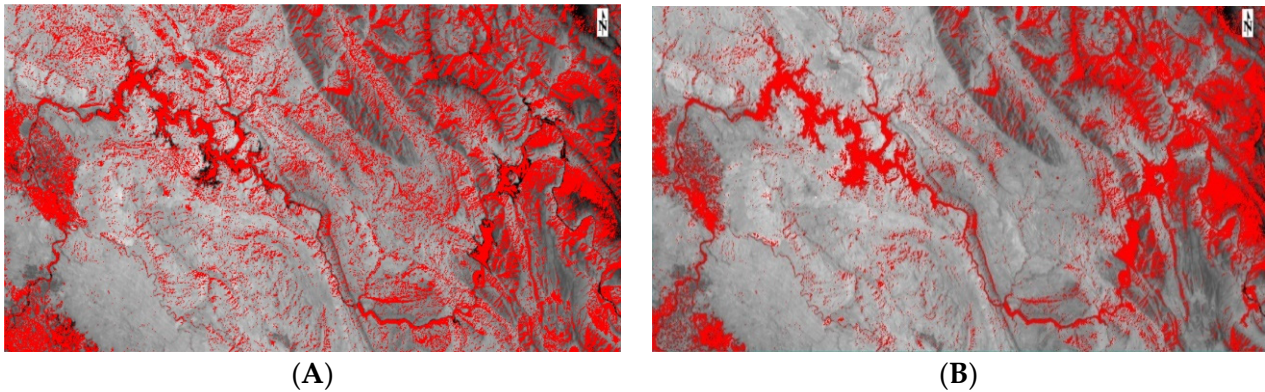


Figure 4. Water mask, in red color, obtained with the ISODATA method. (A) Winter. (B) Summer.

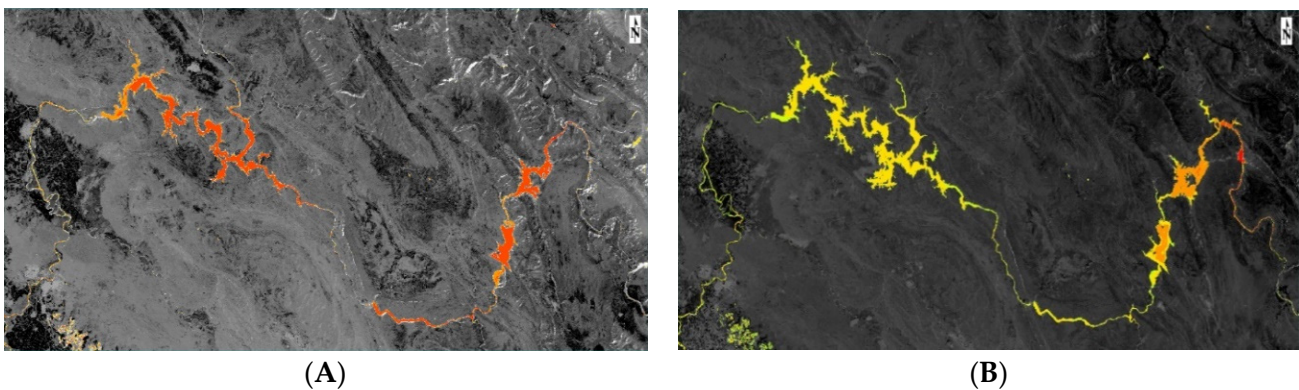


Figure 5. Water mask obtained with NDWI method. (A) Winter (water showed in orange color). (B) Summer (water in yellow color).

As can be seen from the results, the use of an indexing and thresholding approach requires user supervision, given the geographical location of the region and the numerous features within the images. This approach, especially when applied to areas downstream of dams, has proven to provide a clearer spatial identification of water bodies.

In this study, the emissivity of water was assumed to be 0.9885 based on the work of Simon et al. [45]. In addition, the values of L_{λ}^{up} , $L_{\lambda}^{\text{down}}$, and t were obtained using the online atmospheric correction parameter calculation tool. This tool takes into account the sensor type, the geographical location of the study area, and the image acquisition time (see Figure 6). Finally, the water temperature was calculated using the corrected surface radiance ($L_{\lambda(T_s)}$) and thermal band constants according to Equation (8) [46].

$$T_s = \frac{K_2}{\ln\left(\frac{K_1}{L_{\lambda(T_s)} + 1}\right)} - 273.15 \quad (8)$$

where T_s represents the temperature of water in Celsius; K_1 and K_2 are the thermal band constants with values of 774/8853 $\text{W} \cdot \text{m}^{-2} \cdot \text{sr} \cdot \text{mm}$ and 1321/0789 respectively; and $L_{\lambda(T_s)}$ is the corrected surface radiance in radians.

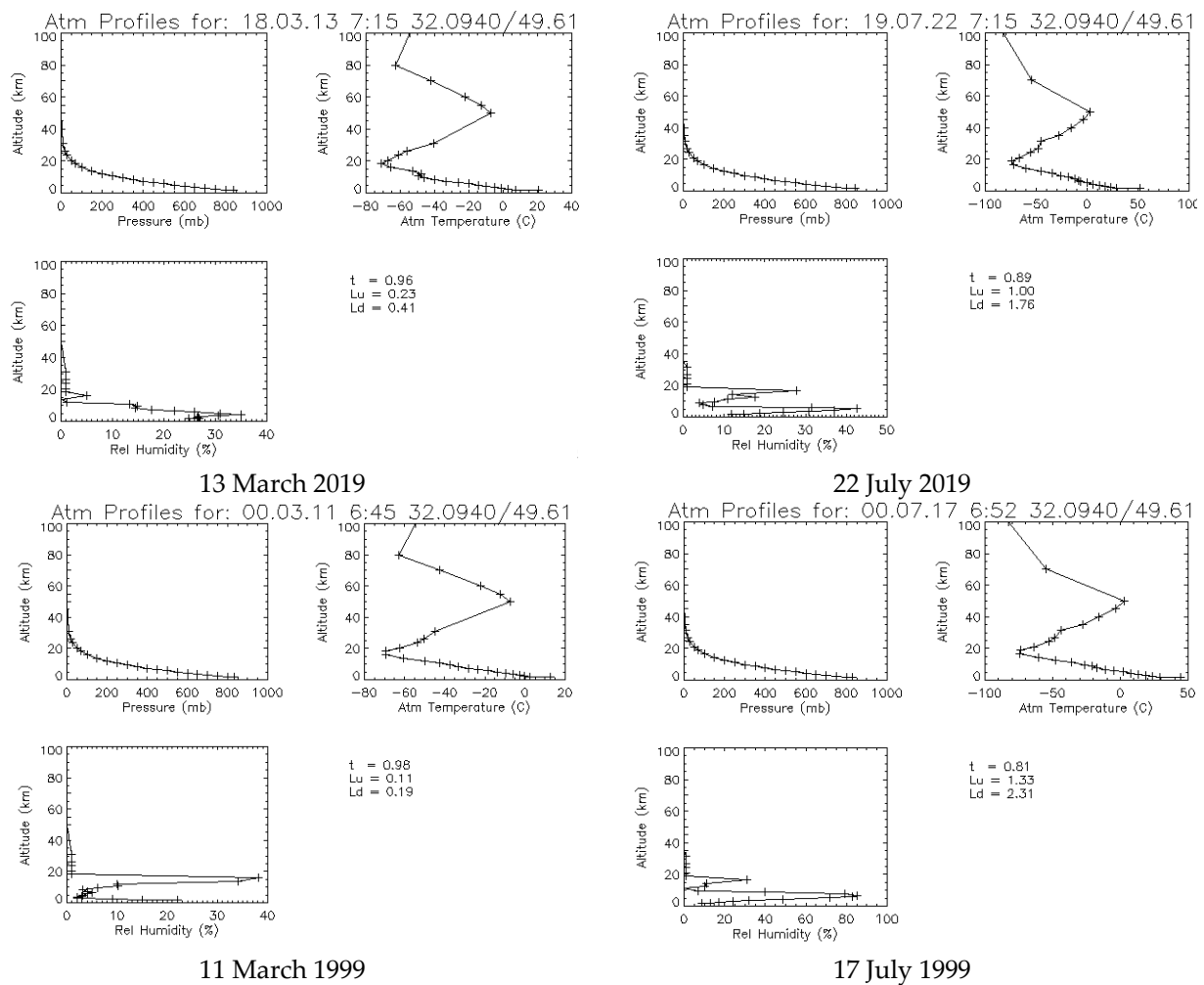


Figure 6. Parameters of atmospheric corrections related to the selected images. Note: t represents the atmospheric transmittance, Lu is the atmospheric path radiance, and Ld is the sky radiance (see Equation (7)).

3.2. Experiments and Results

After applying radiometric and atmospheric improvements to the satellite images, the river water temperature image for the Karun River was generated. Before analyzing the graphs, it is important to note that the Landsat-8 thermal images have a spatial resolution of 100 m, as explained above. Consequently, the rivers studied should have a minimum width of 200-to-300 m in order to allocate at least two or three pixels in the thermal image. It is recommended to focus on areas where the river width in the thermal image is at least three pixels [12,13].

There are many features in different scenes of the image, such as urban, agricultural, mountainous, and aquatic areas. A manual profile of temperature fluctuations along the dam and river course was accomplished by selecting water pixels, constituting a non-systematic method. In addition, the width of the river, which ranges from 150 to 300 m, increases the likelihood of selecting non-water pixels, especially in areas where the river's width is less than three pixels. Therefore, in order to decrease the human error associated with the incorrect selection of pixels along the longitudinal profile drawing, it is essential to apply a masking operation to separate non-water features from water features. For this reason, the generated water mask in Figure 5 was transformed into a binary image using a threshold, as shown in Figure 7, to separate non-water areas from water areas.

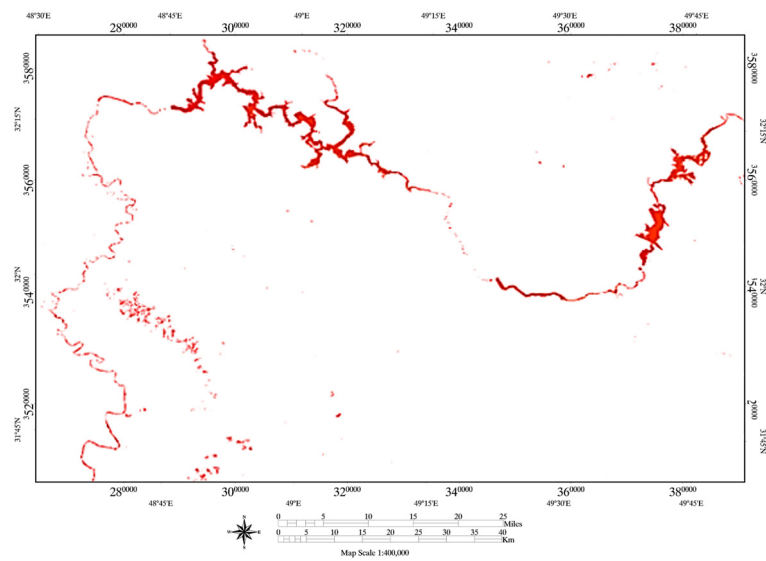


Figure 7. The water mask of the Karun River and the Gotvand and Shahid Abbaspour Dams.

After creating the water temperature map for the study area, the map of temperature changes was generated. Thus, Figure 8 shows the map of temperature changes in the Karun River and its surroundings during the summer and winter seasons. Longitudinal profiles or histograms were then drawn on the temperature change map, allowing us to observe great temperature differences in summer, while moderate changes in this variable were registered during winter. This situation can be verified in each studied dam in Figure 9.

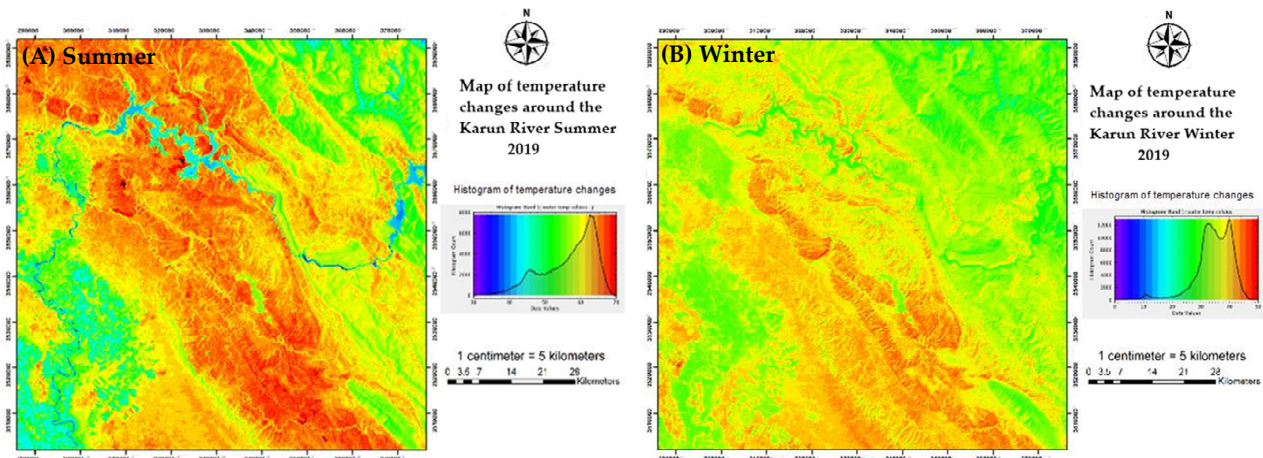


Figure 8. Map of temperature changes in the Karun River in 2019. (A) Summer. (B) Winter.

Likewise, our analysis of the spatial and temporal patterns of water temperature using Landsat OLI thermal infrared imagery reveals a significant impact of the dams studied on river temperature. Figure 9 shows the temperature values at the locations of the Gotvand and Shahid Abbaspour Dams during summer and winter. As can be seen from the graphs, the water temperature upstream of the dams shows negligible variations due to the static and immobile nature of the water. However, downstream of the dams, the water temperature undergoes more significant changes. In summer, when water is released from the upstream reservoir, the water temperature drops. In contrast, in winter, the temperature downstream of the dams remains relatively stable and almost the same as upstream.

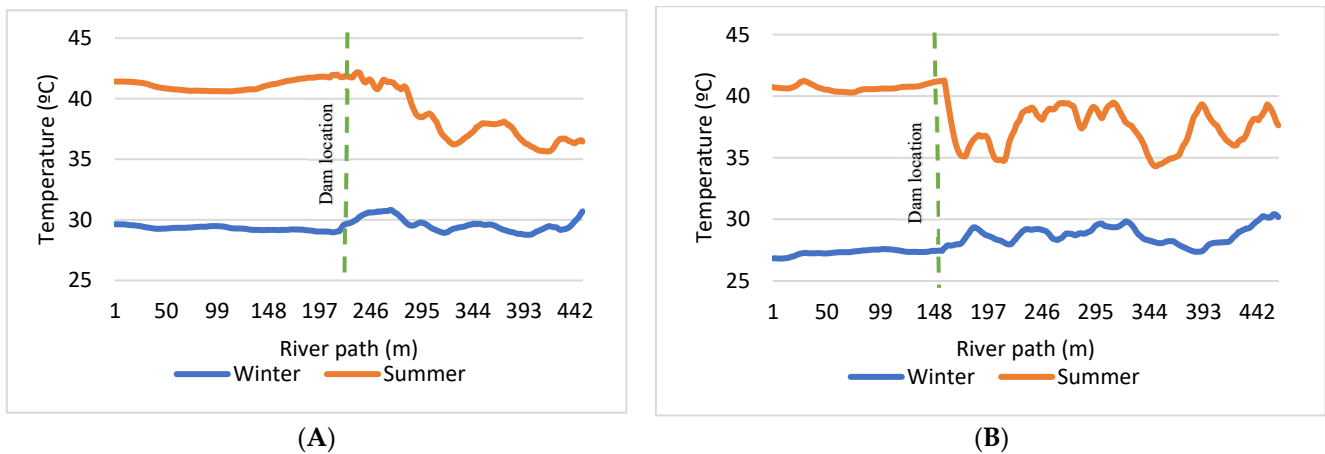


Figure 9. Changes in the water temperature at (A) Shahid Abbaspour Dam in 2019 and (B) Gotvand Dam in 2019.

Temperature change graphs, categorized by dam, are presented in Figure 9, with summer temperature change profiles shown in orange and winter temperature change profiles shown in blue. In Figure 9A, the average water temperature upstream of Shahid Abbaspour Dam is about 41 degrees Celsius in the summer and about 37 degrees Celsius downstream. In winter, the average water temperature upstream is about 27 degrees Celsius, and downstream, it is about 28 degrees Celsius. In Figure 9B, the average water temperature upstream of Gotvand Dam is about 41 degrees Celsius in summer and about 38 degrees Celsius downstream. In winter, the average water temperature upstream is about 29 degrees Celsius, and downstream, it is about 30 degrees Celsius.

The graphs and results show that the Shahid Abbaspour Dam causes the river water's temperature to be about 4 degrees Celsius cooler in summer and about 1 degree Celsius warmer in winter. Similarly, the Gotvand Dam gives similar results to the Shahid Abbaspour Dam, causing the river water to be about 3 degrees Celsius cooler in summer and about 1 degree Celsius warmer in winter. These two dams, Gotvand and Shahid Abbaspour, are about 70 km apart and have similar effects on the Karun River. This suggests that, after passing through the Shahid Abbaspour Dam, the water temperature decreases, and then it increases between the Shahid Abbaspour Dam and the reservoir of the Gotvand Dam, until it returns to its original temperature. Subsequently, passing through the Gotvand Dam leads to a decrease in water temperature.

The assessments were repeated on Landsat-5 imagery to examine the impact of the dams on temperature changes over a 20-year period. The results of water temperature changes in 1999–2000 for both summer and winter are shown in Figure 10. The orange profile corresponds to temperature changes in summer, and the blue profile represents the winter season. In summer, the average water temperature upstream of Shahid Abbaspour Dam is about 50 degrees Celsius. When the water is released, the water temperature downstream reaches about 45 degrees Celsius, and over time, as it moves away from the dam, it first drops to about 36 degrees Celsius and then gradually rises. In winter, the average water temperature upstream is about 23 degrees Celsius, reaching about 25 degrees Celsius downstream after the water is released.

At the Shahid Abbaspour Dam, the discharged water is about 5 degrees Celsius cooler in summer and about 2 degrees Celsius warmer in winter. This pattern of temperature change repeats itself. The pattern of temperature changes in the Karun River for Landsat-5 imagery in the years 1999–2000 is consistent with Landsat-8 imagery in the years 2018–2019, showing a recurring pattern. This suggests that the presence of dams has a noteworthy impact on the temperature of the river.

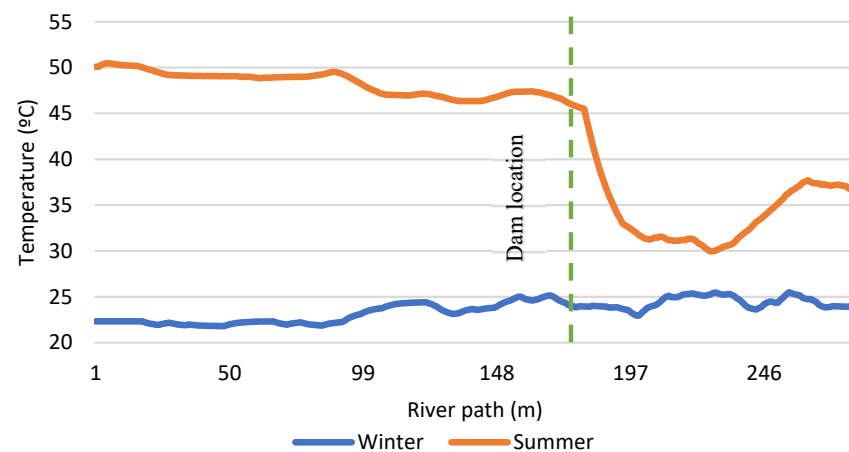


Figure 10. Changes in water temperature in the Shahid Abbaspour Dam in 1999–2000.

In summer, when the natural flow of the river is low, it is not possible to supply air to the lower layers. As a result, multiple layers of water form, with warmer water at the top and colder water at the bottom. Oxygen decreases in these layers. As these layers are very cold and their dissolved oxygen content is low, an increase in temperature provides a favorable environment for bacterial growth and pollution. However, in winter, the temperature of the upper layers often drops, and there is less stratification than in summer. Therefore, the water temperature downstream of the dams can change suddenly because the water behind the dam has a different temperature due to thermal stratification.

After investigating the impact of the dam on temperature changes in the Karun River, the impact of urban, agricultural, and industrial areas on temperature changes was also investigated. The analysis shown in Figure 11 identified areas that caused temporary and unusual increases in water temperature, and the temperature changes are shown in Figures 12 and 13. Through visual interpretation of the temperature map in Figure 11A along the Karun River from the Gotvand Dam to the Jannat Makan and Somaleh regions, transient temperature increases were observed at some points. It is worth noting that the areas identified in Figure 11 present several urban, agricultural, and industrial pollution zones. Due to the increasing scarcity of water resources in arid and semi-arid regions, this situation is becoming more frequent [47,48].

Figure 11B shows the temperature variation map of the Karun River in the Shushtar urban area, highlighting the impact of urban and industrial zones on temperature variation. Through a visual interpretation of the map, it can be observed that instantaneous temperature increases occur at some points. These instantaneous increases are considerably related to water discharges from industrial zones which elevate the average temperature of this river [21,22].

Rivers are one of the chief sources of water for various purposes, including agriculture, industry, and drinking. However, they are also among the most common sources of pollution, especially in arid and semi-arid areas [1,2]. The Karun River, the most important surface water source in Khuzestan Province and the country, is no exception, receiving pollution from urban, agricultural, and industrial sources. The country's heavy industrial complexes, located in five industrial zones along the Karun River, contribute significantly to the pollution of the river. Industrial effluents from the cities of Abadan, Dezful, Masjed Soleyman, Khorramshahr, and Shushtar are discharged into the Karun River. Irrigation networks, drainage, and cultivation play an important role in ensuring global food security. The return flow of water from agricultural, drinking, and aquaculture uses poses a challenge to water resources in terms of quality.

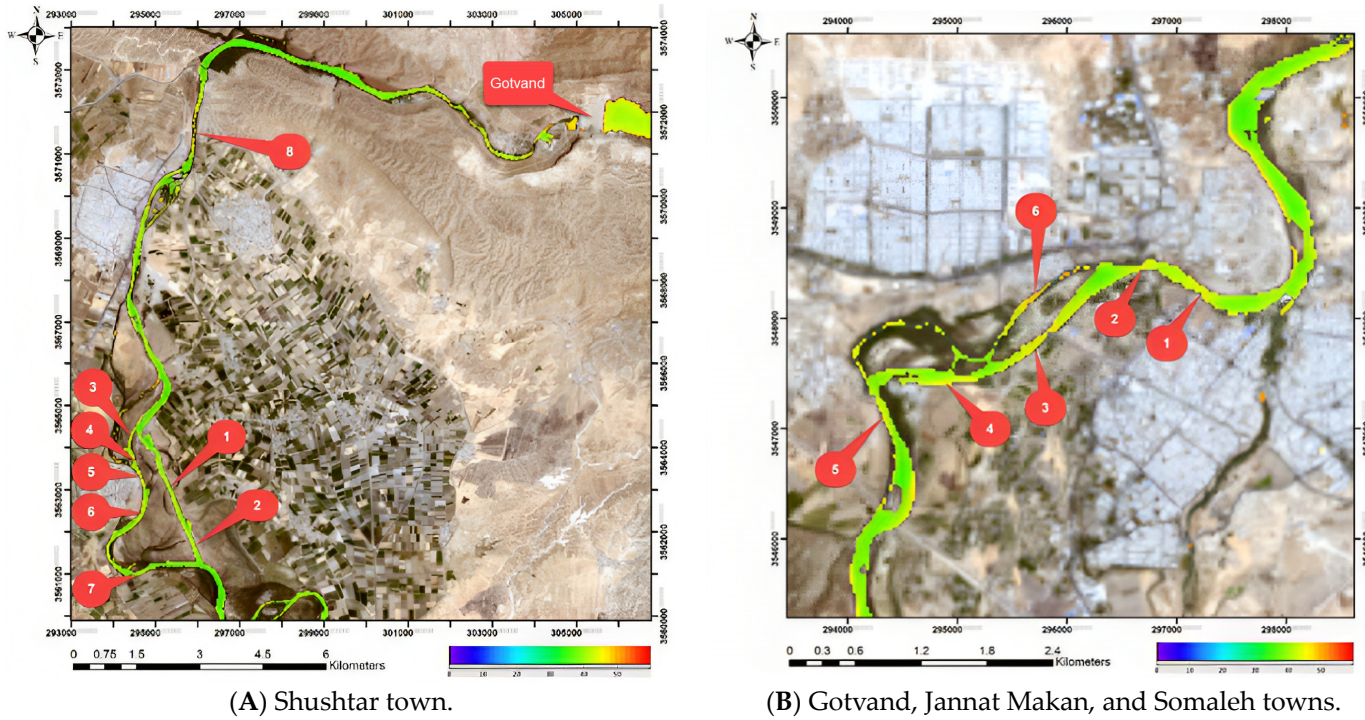


Figure 11. Areas surveyed for thermal pollutants: (A) Shushtar town, where points depict transient temperature increases. (B) The towns of Gotvand, Jannat Makan, and Somaleh towns, where points depict instantaneous temperature increases.

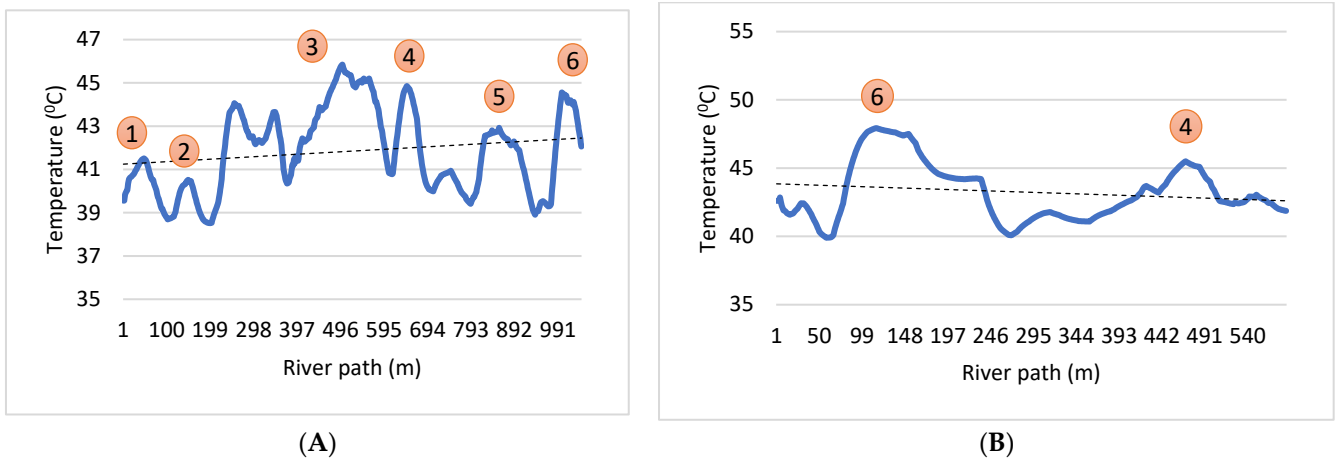


Figure 12. Profiles of the temperature changes caused by the urban areas and industrial areas (Shushtar) (according to Figure 11A) and their average temperature trends. (A) Changing water temperatures in relation to Landsat-8 imagery in 2019. (B) Changing water temperatures in relation to Landsat-5 imagery in 1999.

After passing through the Gotvand Dam, the Karun River flows through towns such as Gotvand, Jannat Makan, Somaleh, and Shushtar before reaching Ahvaz. As mentioned above, urban, agricultural, and industrial pollution affects this river, leading to an increase in water temperature [20–22]. One of the methods used to identify and monitor pollution sources on a regular and continuous basis is the use of thermal maps generated from satellite imagery.

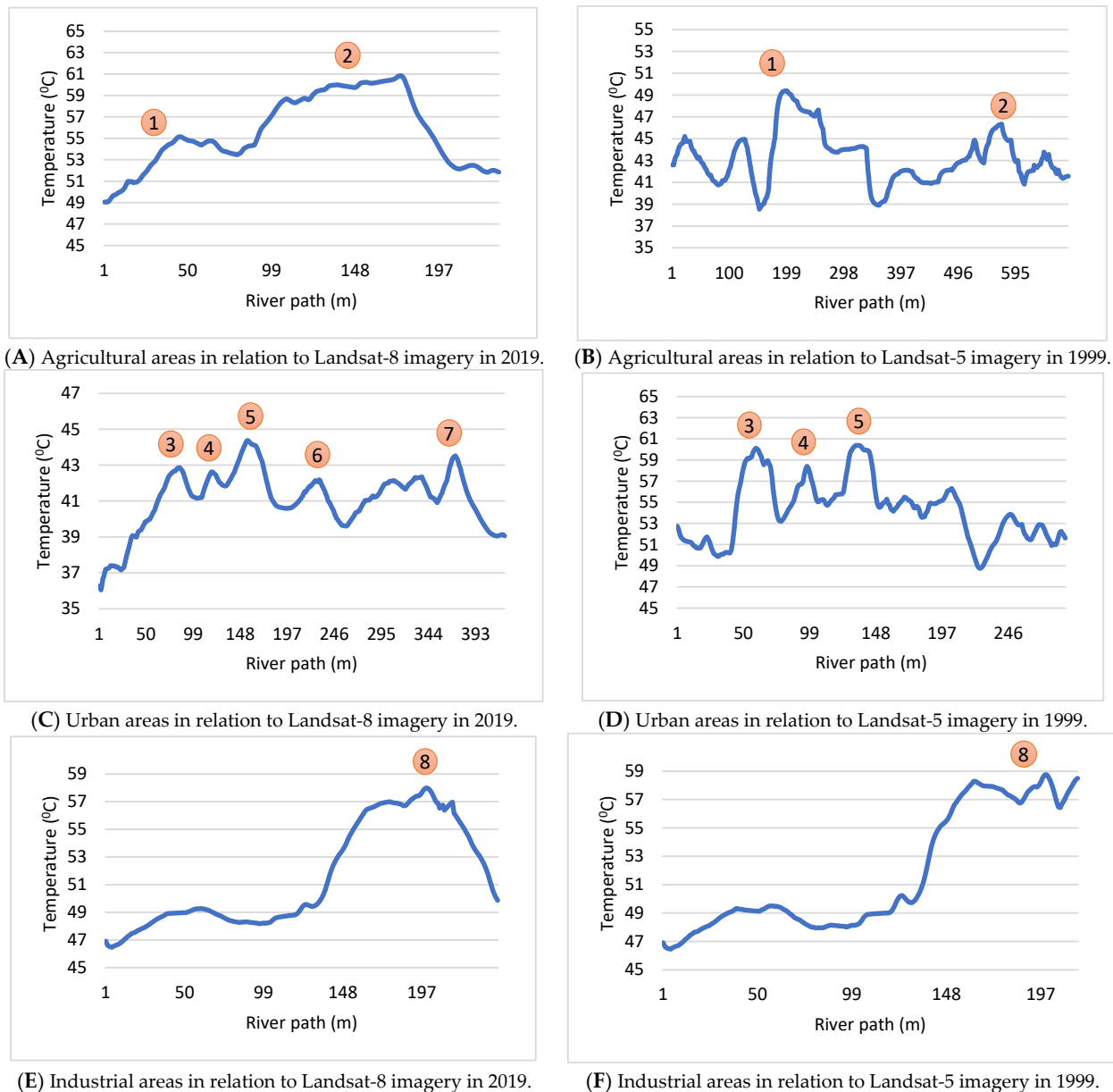


Figure 13. Profiles of the temperature changes caused by the urban areas, the agricultural areas, and the industrial areas (Gotvand, Jannat Makan, and Somaleh) (according to Figure 11B).

To complement the visual interpretation of the thermal pollution maps of urban, agricultural, and industrial areas shown in Figure 11, temperature change profiles were drawn according to the identified regions in Figures 12 and 13. The process of drawing temperature change profiles in 2019 and 1999 using Landsat-8 and Landsat-5 satellite imagery was undertaken to identify and compare areas along the Karun River where water temperature is unusually increasing over a 20-year period. A comparison of the temperature change diagrams and the results of water temperature changes in the Gotvand, Jannat Makan, and Shushtar areas over the 20-year period revealed almost identical patterns, indicating the continued presence of most of these pollution sources from 1999 to the 2019. According to the obtained results (Figure 12), a clear surge in the average water temperature in the river was estimated in 2019, whereas, in 1999, this increasing trend was not observed.

4. Discussion

The rising water temperatures of rivers are a major environmental hazard, directly and indirectly affecting the climate of neighboring regions, aquatic ecosystems, etc., but are scarcely studied regarding other causes of surface and groundwater contamination, such as chemical loads from industry or agriculture [48–55]. The considered remote sensing sources have been demonstrated to be useful tools to detect and quantify temperature changes in rivers, and the same goes for numerous water and environmental bodies (such as aquifers, wetlands, agricultural plots, etc.) that usually depict the same limitation to apply remote sensing data: the reduced spatial size of these elements, which encompass low pixels from the mentioned satellite sources [56–60]. Therefore, studying, investigating, and presenting appropriate solutions in this area can be very useful and practical to the scientific community and to local authorities. Historical water temperature data over large regions and long time periods are usually not readily available, owing to the restricted number of ground-based sensors [49,51]. Even if rivers and dams are equipped with sensors for water temperature, the supposition that data collected by one or more ground-based sensor at scarce different locations offer sufficient information about the spatial distribution of the overall water temperature in the studied area may not hold in practice [53]. In this study, a large area of the Karun River was studied over a long period of time, using remotely sensed imagery.

The results suggest that the use of remote sensing data effectively overcomes the limitations and shortcomings of ground-based sensors for estimating water temperature and identifying pollution areas. It provides experts with spatially extensive and highly synchronized data. Thermal pollution from dams has a significant impact on the downstream river environment and ecology [48–52]. A case study using Landsat-8 imagery (during the period 2018–2019) shows that the Shahid Abbaspour and Gotvand Dams lead to a decrease in downstream water temperature (Figure 9). After the Shahid Abbaspour Dam ends, the water temperature is about 4 degrees Celsius cooler in summer and remains relatively constant in winter (about 1 degree Celsius warmer). The Gotvand Dam shows similar results, with water temperatures about 3 degrees Celsius cooler in summer and about 1 degree Celsius warmer in winter. The monitoring of the Gotvand Dam was repeated over a period of 20 years, using Landsat-5 images (during the period 1999–2000). The water temperature is about 5 degrees Celsius cooler in summer and about 2 degrees Celsius warmer in winter when water is released upstream. These results are consistent with the findings for the period 2018–2019.

In addition to the effects derived from dams or reservoirs on streams and related ecosystems [49,61], other factors commonly contribute to the pollution of rivers, such as urban, agricultural, and industrial pollutants [48–51,62]. The discharge of pollutants into rivers not only increases chemical pollution [1,48] but also increases water temperature [49,63]. As shown in Figures 12 and 13, these pollutants have been discharged into the river and have caused an increase in water temperature. The accessibility and volume of these pollutants have facilitated their entry into rivers [52–54]. By analyzing the results of temperature changes along the Karun River, it can be concluded that the pollutant sources that were present in 1999 continue to increase the temperature of the Karun River to this day (over a twenty-year period). The introduction of pollutant sources into rivers during these years highlights the need to use novel and cost-effective monitoring methods to control the reduction of pollutant sources and to seriously reconsider how polluted areas are identified and monitored.

5. Conclusions

Thermal contamination is the reduction of water quality caused by any process altering the ambient temperature of the water. Monitoring water resources traditionally relies on ground-based sensors and field measurements to simulate water quality and identify pollutants. Nevertheless, these methods are often expensive, time-consuming, and limited by the number of sensors, as well as spatial and temporal constraints.

To address these challenges, this research proposes an economical and cost-effective approach for monitoring thermal pollution in the Karun River. This method utilizes free remote sensing imagery, specifically the thermal bands of Landsat-8 and Landsat-5 satellites. The selection of the Karun River for this work is justified by the existence of numerous dams along its course and its expansive estuary. This study focused on the Shahid Abbaspour Dam (Karun 1) and the Gotvand Dam over a 20-year period to estimate the surface water temperature. The findings reveal that the dams exhibit a seasonal impact on the river's temperature. During the summer, low natural flow behind the dam inhibits the air from reaching the underlying layers, causing thermal stratification in the water. Consequently, water flowing downstream is much colder than the river's water, resulting in lower temperatures downstream of the dams compared to the reservoir's upstream surface water temperature.

After examining the dams' effect on temperature changes, this study investigated the influence of urban, agricultural, and industrial areas on temperature fluctuations. The Gotvand Dam area in the Jannat Makan region and Shushtar town along the Karun River were selected for visual interpretation. Urban, agricultural, and industrial facilities were identified, pinpointing temperature increases. Temperature change profiles for these areas were plotted using satellite imagery for 2019 and 1999. Comparing the temperature change graphs over the 20-year period revealed consistent patterns in polluted areas, indicating the sustained presence of pollutant sources over time. Moreover, the number of these sources has increased to the present day.

In general, the results of this study indicate that satellite data can be useful as an accessible and free source for monitoring thermal pollution and temperature changes over time and space. However, these temperature changes may vary depending on different factors and pollutant sources, and they may show seasonal or permanent behavior. This aspect should be taken into account in the planning and monitoring processes.

Author Contributions: Conceptualization, R.N., A.K. and S.J.; data curation, R.N. and A.K.; formal analysis, R.N., A.K., S.J. and S.B.H.S.A.; project administration, A.K.; software, R.N.; supervision, A.K. and A.J.-A.; writing—original draft, R.N., A.K., S.J., S.B.H.S.A. and P.M.; writing—review and editing, R.N., A.K., S.J., S.B.H.S.A., P.M. and A.J.-A. All authors have read and agreed to the published version of the manuscript.

Funding: This research received no external funding.

Institutional Review Board Statement: Not applicable.

Informed Consent Statement: Not applicable.

Data Availability Statement: Data are contained within the article.

Acknowledgments: Antonio Jodar-Abellan acknowledges resources from the *Margarita Salas* Postdoc Spanish Program and from the scientific project AGROALNEXT2022/NAC/00086. In the same way, the authors acknowledge the reviewers' comments about the present manuscript, as well as the editor's assistance.

Conflicts of Interest: The authors declare that they have no known competing financial interests or personal relationships that could have appeared to influence the work reported in this paper.

References

1. Asadollah, S.B.H.S.; Sharafati, A.; Motta, D.; Yaseen, Z.M. River water quality index prediction and uncertainty analysis: A comparative study of machine learning models. *J. Environ. Chem. Eng.* **2021**, *9*, 104599. [[CrossRef](#)]
2. Todeschini, S.; Papiri, S.; Sconfietti, R. Impact assessment of urban wet-weather sewer discharges on the Vernavola river (Northern Italy). *Civ. Eng. Environ. Syst.* **2011**, *28*, 209–229. [[CrossRef](#)]
3. Ehteram, M.; Sharafati, A.; Asadollah, S.B.H.S.; Neshat, A. Estimating the transient storage parameters for pollution modeling in small streams: A comparison of newly developed hybrid optimization algorithms. *Environ. Monit. Assess.* **2021**, *193*, 475. [[CrossRef](#)] [[PubMed](#)]
4. Vinnå, L.R.; Wüest, A.; Bouffard, D. Physical effects of thermal pollution in lakes. *Water Resour. Res.* **2017**, *53*, 3968–3987. [[CrossRef](#)]

5. Miara, A.; Vörösmarty, C.J.; Macknick, J.E.; Tidwell, V.C.; Fekete, B.; Corsi, F.; Newmark, R. Thermal pollution impacts on rivers and power supply in the Mississippi River watershed. *Environ. Res. Lett.* **2018**, *13*, 34033. [CrossRef]
6. Caissie, D. The thermal regime of rivers: A review. *Freshw. Biol.* **2006**, *51*, 1389–1406. [CrossRef]
7. Hamid, A.; Bhat, S.U.; Jehangir, A. Local determinants influencing stream water quality. *Appl. Water Sci.* **2020**, *10*, 24. [CrossRef]
8. Issakhov, A.; Zhandaulet, Y. Thermal pollution zones on the aquatic environment from the coastal power plant: Numerical study. *Case Stud. Therm. Eng.* **2021**, *25*, 100901. [CrossRef]
9. Abdi, R.; Endreny, T. A river temperature model to assist managers in identifying thermal pollution causes and solutions. *Water* **2019**, *11*, 1060. [CrossRef]
10. Salehi, B.; Jarahizadeh, S.; Sarafraz, A. An improved RANSAC outlier rejection method for UAV-derived point cloud. *Remote Sens.* **2022**, *14*, 4917. [CrossRef]
11. Salehi, B.; Jarahizadeh, S. Improving the UAV-derived DSM by introducing a modified ransac algorithm. *Int. Arch. Photogramm. Remote Sens. Spatial Inf. Sci.* **2022**, XLIII-B2-2022, 147–152. [CrossRef]
12. Wolter, P.T.; Mladenoff, D.J.; Host, G.E.; Crow, T.R. Using multi-temporal landsat imagery. *Photogramm. Eng. Remote Sens.* **1995**, *61*, 1129–1143.
13. Chen, C.; Shi, P.; Mao, Q. Application of remote sensing techniques for monitoring the thermal pollution of cooling-water discharge from nuclear power plant. *J. Environ. Sci. Health Part A* **2003**, *38*, 1659–1668. [CrossRef] [PubMed]
14. Nie, P.; Wu, H.; Xu, J.; Wei, L.; Zhu, H.; Ni, L. Thermal pollution monitoring of Tianwan nuclear power plant for the past 20 years based on Landsat remote sensed data. *IEEE J. Sel. Top. Appl. Earth Obs. Remote Sens.* **2021**, *14*, 6146–6155. [CrossRef]
15. Yavari, S.M.; Qaderi, F. Determination of thermal pollution of water resources caused by Neka power plant through processing satellite imagery. *Environ. Dev. Sustain.* **2020**, *22*, 1953–1975. [CrossRef]
16. Ling, F.; Foody, G.M.; Du, H.; Ban, X.; Li, X.; Zhang, Y.; Du, Y. Monitoring thermal pollution in rivers downstream of dams with Landsat ETM+ thermal infrared images. *Remote Sens.* **2017**, *9*, 1175. [CrossRef]
17. Fazelpoor, K.; Sohrab, A.D.; Elmizadeh, H.; Asgari, H.M.; Khazaei, S.H. The Evaluation of Sea Surface Temperature and the Relationship between SST and Depth in the Persian Gulf by MODIS. 2016. Available online: <https://aquadocs.org/handle/1834/13627> (accessed on 24 November 2023).
18. Medina-Lopez, E.; Ureña-Fuentes, L. High-resolution sea surface temperature and salinity in coastal areas worldwide from raw satellite data. *Remote Sens.* **2019**, *11*, 2191. [CrossRef]
19. Jang, J.-C.; Park, K.-A. High-resolution sea surface temperature retrieval from Landsat 8 OLI/TIRS data at coastal regions. *Remote Sens.* **2019**, *11*, 2687. [CrossRef]
20. Karamouz, M. Waste-Load Allocation Model for Seasonal River Water Quality Management: Application of Sequential Dynamic Genetic Algorithms. 2005. Available online: https://www.sid.ir/en/VEWSSID/J_pdf/95520050209.pdf (accessed on 24 November 2023).
21. Afkhami, M.; Shariat, M.; Jaafarzadeh, N.; Ghadiri, H.; Nabizadeh, R. Developing a water quality management model for Karun and Dez Rivers. *J. Environ. Health Sci. Eng.* **2007**, *4*, 99–106.
22. Karamouz, M.; Kerachian, R.; Akhbari, M.; Hafez, B. Design of river water quality monitoring networks: A case study. *Environ. Model. Assess.* **2009**, *14*, 705–714. [CrossRef]
23. Beychok, M.R. Aqueous Wastes: From Petroleum and Petrochemical Plants. 1967. Available online: <https://cir.nii.ac.jp/crid/113000796726234368> (accessed on 24 November 2023).
24. Scarrott, R.; Reed, D.; Bayliss, A. *Indexing the Attenuation Effect Attributable to Reservoirs and Lakes*; Institute of Hydrology: Wallingford, UK, 1999.
25. Montaldo, N.; Mancini, M.; Rosso, R. Flood hydrograph attenuation induced by a reservoir system: Analysis with a distributed rainfall-runoff model. *Hydrol. Process.* **2004**, *18*, 545–563. [CrossRef]
26. Gioia, A. Reservoir routing on double-peak design flood. *Water* **2016**, *8*, 553. [CrossRef]
27. Sullivan, A.B.; Rounds, S. Modeling Streamflow and Water Temperature in the North Santiam and Santiam Rivers, Oregon, 2001-02. US Geological Survey. 2004. Available online: [https://books.google.com/books?hl=en&lr=&id=O1COADypYwIC&oi=fnd&pg=PA1&dq=Sullivan,+A.+B.+and+S.+Rounds+\(2004\).+Modeling+Streamflow+and+Water+Temperature+in+the+North+Santiam+and+Santiam+Rivers,+Oregon,+2001-02,+US+Department+of+the+Interior,+US+Geological+Survey.&ots=gzrzcmiomv&sig=pFB9adEYIHtaVXz5fAe5X_-NIWU](https://books.google.com/books?hl=en&lr=&id=O1COADypYwIC&oi=fnd&pg=PA1&dq=Sullivan,+A.+B.+and+S.+Rounds+(2004).+Modeling+Streamflow+and+Water+Temperature+in+the+North+Santiam+and+Santiam+Rivers,+Oregon,+2001-02,+US+Department+of+the+Interior,+US+Geological+Survey.&ots=gzrzcmiomv&sig=pFB9adEYIHtaVXz5fAe5X_-NIWU) (accessed on 24 November 2023).
28. Olden, J.D.; Naiman, R.J. Incorporating thermal regimes into environmental flows assessments: Modifying dam operations to restore freshwater ecosystem integrity. *Freshw. Biol.* **2010**, *55*, 86–107. [CrossRef]
29. Preece, R.M.; Jones, H.A. The effect of Keepit Dam on the temperature regime of the Namoi River, Australia. *River Res. Appl.* **2002**, *18*, 397–414. [CrossRef]
30. Steel, E.A.; Lange, I.A. Using wavelet analysis to detect changes in water temperature regimes at multiple scales: Effects of multi-purpose dams in the Willamette River basin. *River Res. Appl.* **2007**, *23*, 351–359. [CrossRef]
31. Wright, S.A.; Anderson, C.R.; Voichick, N. A simplified water temperature model for the Colorado River below Glen Canyon Dam. *River Res. Appl.* **2009**, *25*, 675–686. [CrossRef]
32. Casado, A.; Hannah, D.M.; Peiry, J.; Campo, A.M. Influence of dam-induced hydrological regulation on summer water temperature: Sauce Grande River, Argentina. *Ecohydrology* **2013**, *6*, 523–535. [CrossRef]

33. Cai, H.; Piccolroaz, S.; Huang, J.; Liu, Z.; Liu, F.; Toffolon, M. Quantifying the impact of the Three Gorges Dam on the thermal dynamics of the Yangtze River. *Environ. Res. Lett.* **2018**, *13*, 054016. [CrossRef]
34. Zhao, J.; Li, H.; Cai, X.; Chen, F.; Wang, L.; Yu, D. Long-term (2002–2017) impacts of Danjiangkou dam on thermal regimes of downstream Han River (China) using Landsat thermal infrared imagery. *J. Hydrol.* **2020**, *589*, 125135. [CrossRef]
35. Shareef, M.A.; Toumi, A.; Khenchaf, A. Prediction of water quality parameters from SAR Images by using multivariate and texture analysis models. In *SAR Image Analysis, Modeling, and Techniques XIV*; SPIE: Bellingham, WA, USA, 2014; pp. 363–378. [CrossRef]
36. Gupta, M.; Ghose, M.K.; Sharma, L.P. Application of remote sensing and GIS for landslides hazard and assessment of their probabilistic occurrence—A case study of NH31A between Rangpo and Singtam. *J. Geomat.* **2009**, *3*, 13–17.
37. Boltzmann, L. *Über Die Beziehung Zwischen dem Zweiten Hauptsatze des Mechanischen Wärmethorie und der Wahrscheinlichkeitsrechnung, Respective den Sätzen Über das Wärmegleichgewicht*; Cambridge University Press: Cambridge, UK, 1877.
38. Masek, J.G.; Vermote, E.F.; Saleous, N.E.; Wolfe, R.; Hall, F.G.; Huemmrich, K.F.; Gao, F.; Kutler, J.; Lim, T.K. A Landsat surface reflectance dataset for North America, 1990–2000. *IEEE Geosci. Remote Sens. Lett.* **2006**, *3*, 68–72. [CrossRef]
39. Chander, G.; Markham, B.L.; Helder, D.L. Summary of current radiometric calibration coefficients for Landsat MSS, TM, ETM+, and EO-1 ALI sensors. *Remote Sens. Environ.* **2009**, *113*, 893–903. [CrossRef]
40. Roy, D.P.; Ju, J.; Kline, K.; Scaramuzza, P.L.; Kovalsky, V.; Hansen, M.; Loveland, T.R.; Vermote, E.; Zhang, C. Web-enabled Landsat Data (WELD): Landsat ETM+ composited mosaics of the conterminous United States. *Remote Sens. Environ.* **2010**, *114*, 35–49. [CrossRef]
41. Hu, Y.; Liu, L.; Liu, L.; Peng, D.; Jiao, Q.; Zhang, H. A Landsat-5 atmospheric correction based on MODIS atmosphere products and 6S model. *IEEE J. Sel. Top. Appl. Earth Obs. Remote Sens.* **2013**, *7*, 1609–1615. [CrossRef]
42. Nguyen, H.C.; Jung, J.; Lee, J.; Choi, S.-U.; Hong, S.-Y.; Heo, J. Optimal atmospheric correction for above-ground forest biomass estimation with the ETM+ remote sensor. *Sensors* **2015**, *15*, 18865–18886. [CrossRef] [PubMed]
43. Barsi, J.A.; Schott, J.R.; Palluconi, F.D.; Hook, S.J. Validation of a web-based atmospheric correction tool for single thermal band instruments. In *Earth Observing Systems X*; SPIE: Bellingham, WA, USA, 2005; pp. 136–142. [CrossRef]
44. Barsi, J.A.; Barker, J.L.; Schott, J.R. An Atmospheric Correction Parameter Calculator for a Single Thermal Band Earth-Sensing Instrument. In Proceedings of the 2003 IEEE International Geoscience and Remote Sensing Symposium, Toulouse, France, 21–25 July 2003; IEEE: Piscataway, NJ, USA, 2003; pp. 3014–3016. Available online: <https://ieeexplore.ieee.org/abstract/document/1294665/> (accessed on 27 November 2023).
45. Simon, R.N.; Tormos, T.; Danis, P.-A. Retrieving water surface temperature from archive LANDSAT thermal infrared data: Application of the mono-channel atmospheric correction algorithm over two freshwater reservoirs. *Int. J. Appl. Earth Obs. Geoinf.* **2014**, *30*, 247–250. [CrossRef]
46. Chander, G.; Markham, B.L.; Barsi, J.A. Revised Landsat-5 thematic mapper radiometric calibration. *IEEE Geosci. Remote Sens. Lett.* **2007**, *4*, 490–494. [CrossRef]
47. Derdour, A.; Jodar-Abellan, A.; Ghoneim, S.S.M.; Almaliki, A.H.; Hussein, E.E.; Pardo, M.A. Groundwater quality assessment for sustainable human consumption in arid areas based on GIS and water quality index in the watershed of Ain Sefra (SW of Algeria). *Environ. Earth Sci.* **2023**, *82*, 510. [CrossRef]
48. Ma, J.; Huang, K. Examining the Factors Influencing Agricultural Surface Source Pollution in the Yangtze River Economic Zone from the Perspectives of Government, Enterprise, and Agriculture. *Sustainability* **2023**, *15*, 14753. [CrossRef]
49. Sinokrot, B.A.; Stefan, H.G. Stream temperature dynamics—Measurements and modeling. *Water Resour. Res.* **1993**, *29*, 2299–2312. [CrossRef]
50. Liang, X.; Pan, Y.; Li, C.; Wu, W.; Huang, X. Evaluating the Influence of Land Use and Landscape Pattern on the Spatial Pattern of Water Quality in the Pearl River Basin. *Sustainability* **2023**, *15*, 15146. [CrossRef]
51. Webb, B.W.; Hannah, D.M.; Moore, R.D.; Brown, L.E.; Nobilis, F. Recent advances in stream and river temperature research. *Hydrol. Process.* **2008**, *22*, 902–918. [CrossRef]
52. Song, W.; Wang, S.; Zhao, J.; Xu, S.; Zhou, X.; Zhang, Y. Comprehensive Treatment for River Pollution in a Coastal City with a Complex River Network: A Case Study in Sanya, China. *Sustainability* **2023**, *15*, 6830. [CrossRef]
53. Vatland, S.J.; Gresswell, R.E.; Poole, G.C. Quantifying stream thermal regimes at multiple scales: Combining thermal infrared imagery and stationary stream temperature data in a novel modeling framework. *Water Resour. Res.* **2015**, *51*, 31–46. [CrossRef]
54. Ma, T.-F.; Wu, J.; Yu, Y.-C.; Chen, T.-T.; Yao, Y.; Liao, W.-L.; Feng, L.; Pan, J. An Assessment of the Heavy Metal Contamination, Risk, and Source Identification in the Sediments from the Liangtan River, China. *Sustainability* **2023**, *15*, 16228. [CrossRef]
55. Todeschini, S.; Papiri, S.; Ciaponi, C. Placement Strategies and Cumulative Effects of Wet-weather Control Practices for Intermunicipal Sewerage Systems. *Water Resour. Manag.* **2018**, *32*, 2885–2900. [CrossRef]
56. Derdour, A.; Jodar-Abellan, A.; Melián-Navarro, A.; Bailey, R.T. Assessment of Land Degradation and Droughts in an Arid Area Using Drought Indices, the Modified Soil-Adjusted Vegetation Index, and Landsat Remote Sensing Data. *Geogr. Res. Lett.* **2023**, *49*, 65–81. [CrossRef]
57. Hunink, J.E.; Eekhout, J.P.C.; Vente, J.D.; Contreras, S.; Droogers, P.; Baille, A. Hydrological Modelling using Satellite-Based Crop Coefficients: A Comparison of Methods at the Basin Scale. *Remote Sens.* **2017**, *9*, 174. [CrossRef]

58. Aznarez, C.; Jimeno-Sáez, P.; López-Ballesteros, A.; Pacheco, J.P.; Senent-Aparicio, J. Analysing the Impact of Climate Change on Hydrological Ecosystem Services in Laguna del Sauce (Uruguay) Using the SWAT Model and Remote Sensing Data. *Remote Sens.* **2021**, *13*, 2014. [[CrossRef](#)]
59. Schubert, H.; Caballero-Calvo, A.; Rauchecker, M.; Rojas-Zamora, O.; Brokamp, G.; Schütt, B. Assessment of Land Cover Changes in the Hinterland of Barranquilla (Colombia) Using Landsat Imagery and Logistic Regression. *Land* **2018**, *7*, 152. [[CrossRef](#)]
60. Seyed-Asadollah, S.B.H.; Sharafati, A.; Motta, D.; Jodar-Abellan, A.; Pardo, M.A. Satellite-based prediction of surface dust mass concentration in southeastern Iran using an intelligent approach. *Stoch. Environ. Res. Risk Assess.* **2023**, *37*, 3731–3745. [[CrossRef](#)]
61. Eekhout, J.; Boix-Fayos, C.; Perez-Cutillas, P.; de Vente, J. The impact of reservoir construction and changes in land use and climate on ecosystem services in a large Mediterranean catchment. *J. Hydrol.* **2020**, *590*, 125208. [[CrossRef](#)]
62. Moussaoui, T.; Derdour, A.; Hosni, A.; Ballesta-de los Santos, M.; Legua, P.; Pardo-Picazo, M.Á. Assessing the Quality of Treated Wastewater for Irrigation: A Case Study of Ain Sefra Wastewater Treatment Plant. *Sustainability* **2023**, *15*, 11133. [[CrossRef](#)]
63. Souaissi, Z.; Ouarda, T.B.M.J.; St-Hilaire, A. Regional thermal index model for river temperature frequency analysis in ungauged basins. *Environ. Model. Softw.* **2023**, *164*, 105709. [[CrossRef](#)]

Disclaimer/Publisher's Note: The statements, opinions and data contained in all publications are solely those of the individual author(s) and contributor(s) and not of MDPI and/or the editor(s). MDPI and/or the editor(s) disclaim responsibility for any injury to people or property resulting from any ideas, methods, instructions or products referred to in the content.